Assessment of the Added Value of Multiscale Modeling of Concrete for Structural Analysis of Segmental Tunnel Rings

Jiao-Long Zhang, Tongji University, Shanghai, China and TU Wien, Vienna, Austria
Eva Binder, Tongji University, Shanghai, China; TU Wien, Vienna, Austria; and Linnaeus University, Växjö, Sweden
Xian Liu and Yong Yuan, Tongji University, Shanghai, China
Herbert Mang, Tongji University, Shanghai, China and TU Wien, Vienna, Austria
Bernhard LA Pichler, TU Wien, Vienna, Austria

Introduction

Concrete is a hierarchically organized material. Its material behavior is related to thermo-hygro-chemo-mechanical processes occurring at its microstructure (Zhang *et al.*, 2013). Thus, it is reasonable to predict its macroscopic properties by making use of information at smaller scales. In the framework of multiscale modeling of concrete, several homogenization methods have been developed, involving e.g., continuum micromechanics (Zaoui, 2002; Bernard *et al.*, 2003), asymptotic expansion techniques (Cui and Yang, 1996; Zhang *et al.*, 2015), lattice approach (Schlangen, 1993), and numerical homogenization by means of the finite element method (Geers *et al.*, 2010). Several homogenization schemes, based on continuum micromechanics, have been developed at the Institute for Mechanics of Materials and Structures of Vienna University of Technology. They allow for estimation of elastic properties (Hellmich and Mang, 2005), strength (Pichler and Hellmich, 2011; Königsberger *et al.*, 2018), creep (Scheiner and Hellmich, 2009; Königsberger *et al.*, 2016), shrink-age (Pichler *et al.*, 2007), and thermal expansion (Wang *et al.*, 2018b) of concrete. In order to assess the added value resulting from the use of such multiscale material models for concrete in the framework of structural analysis of reinforced concrete structures, the authors have been involved in a research project, entitled "Bridging the gap by means of multiscale structural analysis" (Mang, 2015). This contribution refers to a part of the results from this project.

A reliable assessment of the added value of multiscale structural analyses requires a comparison of experimental data with results from both conventional and multi-scale structural analysis, see **Fig. 1**. As for the present contribution, experimental results are taken from a real-scale test of a segmental tunnel ring (**Fig. 2**), carried out at Tongji University. Both conventional and multiscale structural analysis are based on transfer relations, representing analytical solutions of the linear theory of circular arches (Zhang *et al.*, 2018, 2019b, 2020). Concerning conventional structural analysis, the material properties of concrete are obtained from the formulae in the *fib* Model Code 2010 (Taerwe and Matthys, 2013). As regards multiscale structural analysis, micromechanics-based multiscale models are taken from Königsberger *et al.* (2018) and Hlobil (2016). This selection is inspired by the previous finding that the performance of these multiscale models for evaluation of early-age material properties of the concrete used for the Hong Kong-Zhuhai-Macao Bridge (HZMB) is significantly better than that based on the *fib* Model Code (Wang *et al.*, 2018a), see **Fig. 3**. This also provides the motivation to quantify the added value of these multiscale models in the framework of structural analysis.

The main content of the present contribution is as follows: (1) hierarchical organization of the analyzed segmental tunnel ring, (2) evaluation of the material properties of concrete by means of multiscale modeling, (3) estimation of the effective stiffness of elements with crack bands and of crack opening widths, (4) transfer relations representing analytical solutions of the linear theory of circular arches, (5) assessment of the added value of multiscale structural analysis, and (6) conclusions drawn from the present study.

Hierarchical Organization of the Segmental Tunnel Ring

Herein, by segmental tunnel ring, one of the rings tested at Tongji University (Liu *et al.*, 2016; Zhang *et al.*, 2019a) is meant, see **Fig. 2**. The radius of the axis of the ring, R, is equal to 2.925 m. The ring consists of six reinforced concrete segments. The six joints of these segments are positioned at angular coordinates $\varphi_j = \text{i}, 2,\ldots 6$ equal to 8°, 73°, 138°, 222°, 287°, and 352°, where φ denotes the angular coordinate, measured from the center of segment ①. The thickness H and the width B of the segments amount to 35 cm and 1.2 m, respectively.

Both the segments and the microstructure of concrete are hierarchically organized, see **Fig. 4**. At the structural level, the six segments are subdivided into 34 elements. Their tangential length is set equal to the crack spacing $\ell_{cs} \approx 50$cm, obtained from experimental measurements. As regards the element level, each element, consisting of reinforcement and concrete, is either intact or containing one central crack band, flanked by lateral undamaged domains. The reinforcement drawing is contained in (Zhang *et al.*, 2019a). Young's modulus E_s and the yield stress f_y of the reinforcement were equal to 210 GPa and 335 MPa, respectively. The concrete was produced from cement, fly ash, slag, water, sand, and aggregates, see **Table 1** for their dosages. The maximum size of the aggregates, d_{max}, was equal to 2 cm. The uniaxial compressive strength of concrete, f_c, reached 28 days after production, amounted to 58 MPa. Multiscale analysis of concrete involved six scales (Zhang *et al.*, 2019a). Scale I refers to C-S-H gel consisting of gel pores that are embedded in a matrix of solid C-S-H. Scale II is associated with the hydration foam, consisting of C-S-H gel needles and spherical capillary pores filled with water or air. The needles and the pores are randomly distributed in space. Scale III refers to the cement paste, consisting of a matrix of hydrate foam and spherical inclusions, representing unhydrated cement, slag,

 doi:10.1016/B978-0-12-819724-0.00091-4

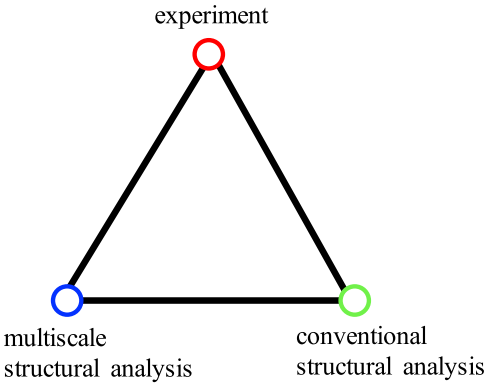

Fig. 1 Triad of results required for an assessment of the added value of multiscale analyses of tunnel segments. Reproduced from Mang, H., 2015. Bridging the gap by means of multiscale structural analyses, Research project supported by the Austrian Science Fund (FWF) P281 31-N32.

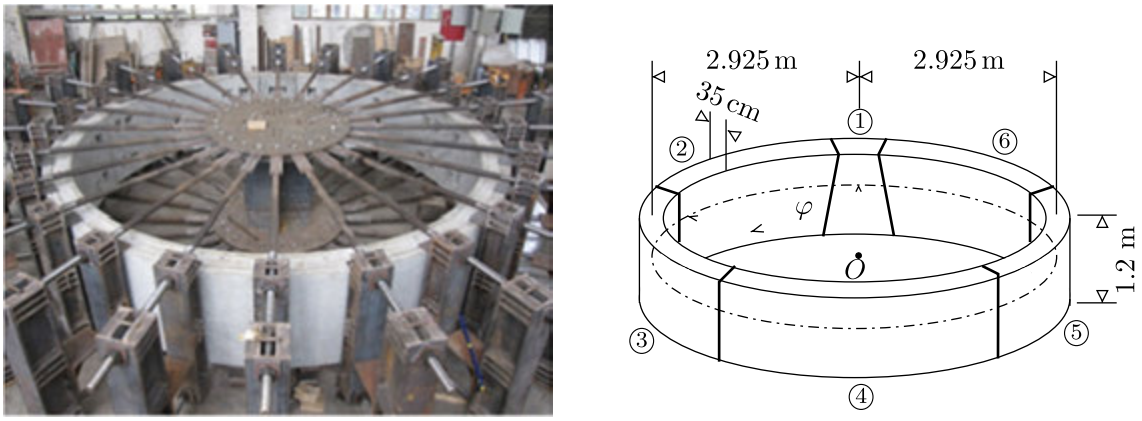

Fig. 2 (a) Photo and (b) geometric dimensions of the investigated segmental tunnel ring according to Liu *et al.* (2016) and Zhang *et al.* (2017), respectively. ①-⑥ are the numbers of the segments, and φ stands for the angular coordinate, measured from the center of the segment ①. According to Liu, X., Bai, Y., Yuan, Y., Mang, H., 2016. Experimental investigation of the ultimate bearing capacity of continuously jointed segmental tunnel linings. Structure and Infrastructure Engineering 12, 1364–1379. Zhang, J.L., Vida, C., Yuan, Y., *et al.*, 2017. A hybrid analysis method for displacement-monitored segmented circular tunnel rings. Engineering Structures 148, 839–856.

and fly ash. Scale IV is associated with the mortar, consisting of a matrix of cement paste and spherical inclusions of sand. Scale V refers to sane concrete, consisting of a matrix of mortar and spherical inclusions of aggregates. Scale VI refers to cracked concrete, containing a matrix of concrete and penny-shaped inclusions of parallel cracks.

Evaluation of the Material Properties of Concrete by Means of Multiscale Modeling

Conventionally, the material properties of concrete can be obtained e.g., from the formulae of the *fib* Model Code 2010 (Taerwe and Matthys, 2013), see details in the Appendix. Based on the experimentally determined compressive strength, $f_c = 58$ MPa, a stress-strain diagram for concrete in tension is obtained, see **Fig. 5(a)**. Alternatively, the material properties of the concrete can also be evaluated by means of multiscale modeling, see **Fig. 5(b)** for the obtained stress-strain diagram. Details are described in the following.

Homogenization of the stiffness and strength of the concrete is carried out, using the model by Königsberger *et al.* (2018). It allows for consideration of the hierarchical organization of the material, the shape, the volume fractions, and the material constants of the heterogeneities, as well as for their mutual interaction at different scales of observation. The hierarchical organization of the material and the shape of the constituents are shown in **Fig. 4**. The corresponding volume fractions of the material constituents of concrete are quantified, based on the initial composition of the concrete, see **Table 1**, and the hydration degrees of cement, fly ash, and slag, see details in (Zhang *et al.*, 2019a). Herein, the hydration degrees ξ of the cement, the slag, and the fly ash are estimated as $\xi_{\text{cement}} = 0.8$ (Termkhajornkit *et al.*, 2014), $\xi_{\text{siag}} = 0.4$ (Lumley *et al.*, 1996), $\xi_{\text{fiyash}} = 0$, respectively, considering that the real-scale test was carried out 28 days after casting of the segments. The mutual interactions of the material constituents are considered in the homogenization schemes. In more detail, matrix-inclusion composites, such as at Scales I, III, IV, and V, are

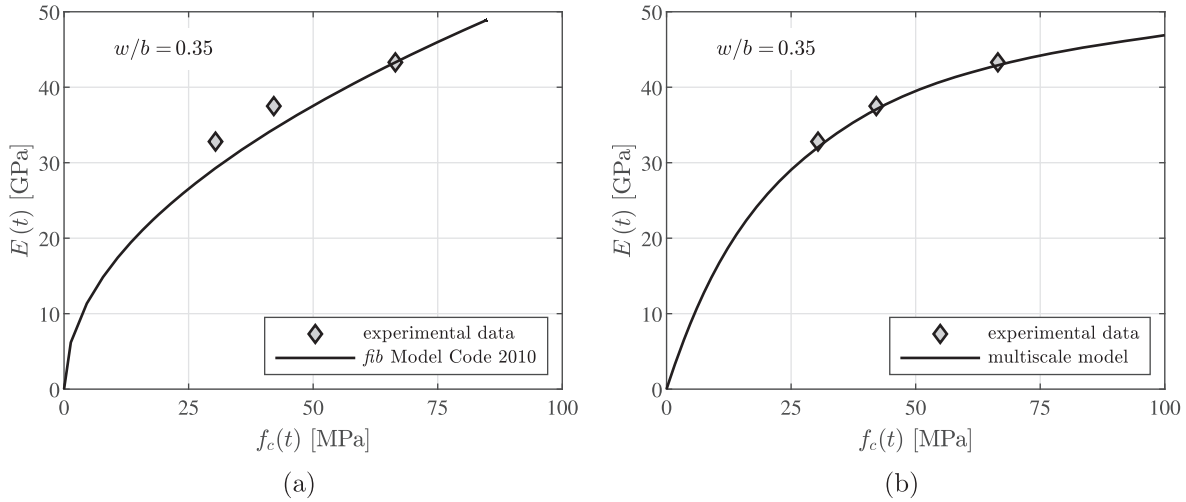

Fig. 3 Correlation between the elasticity modulus E and the compressive strength f_c of the concrete used for the immersed tunnel connecting the two parts of the Hong Kong-Zhuhai-Macao Bridge: (a) comparison of the results from the *fib* Model Code (Taerwe and Matthys, 2013) with the experimental results and (b) comparison of the results from multiscale analysis with the experimental results. Reproduced from Wang, H., Binder, E., Mang, H., Yuan, Y., Pichler, B., 2018a. Multiscale structural analysis inspired by exceptional load cases concerning the immersed tunnel of the Hong Kong-Zhuhai-Macao Bridge. Underground Space 3, 252–267.

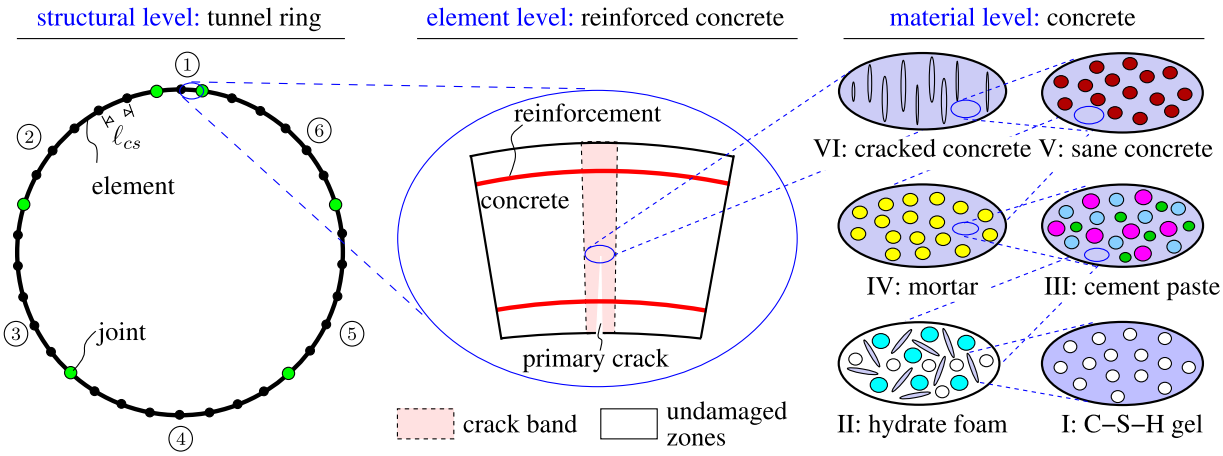

Fig. 4 Multiscale organogram of the segmental tunnel ring, tested at Tongji University. Reproduced from Zhang, J.L., Mang, H.A., Liu, X., Yuan, Y., Pichler, B., 2019a. On a nonlinear hybrid method for multiscale analysis of a bearing-capacity test of a real-scale seg-mental tunnel ring. International Journal for Numerical and Analytical Methods in Geomechanics 43, 1343–1372.

Table 1 Composition of the concrete used for the production of the segments

	Cement	*Fly ash*	*Slag*	*Water*	*Sand*	*Aggregates*
Dosage [kg/m3]	323	67	57	152	631	1169

Note: Zhang, J.L., Mang, H.A., Liu, X., Yuan, Y., Pichler, B., 2019a. On a nonlinear hybrid method for multiscale analysis of a bearing-capacity test of a real-scale seg-mental tunnel ring. International Journal for Numerical and Analytical Methods in Geomechanics 43, 1343–1372.

homogenized, using the Mori-Tanaka scheme (Mori and tanaka 1973, Benveniste, 1987). The polycrystalline microstructure at Scale II is homogenized, using the self-consistent scheme (Hershey, 1954, Kröner, 1958). Homogenization of the elasticity modulus and the uniaxial compressive strength of concrete delivers the following results:

$$E = 43.6\,\text{GPa}, \tag{1}$$

$$f_c = 62.0\text{MPa}. \tag{2}$$

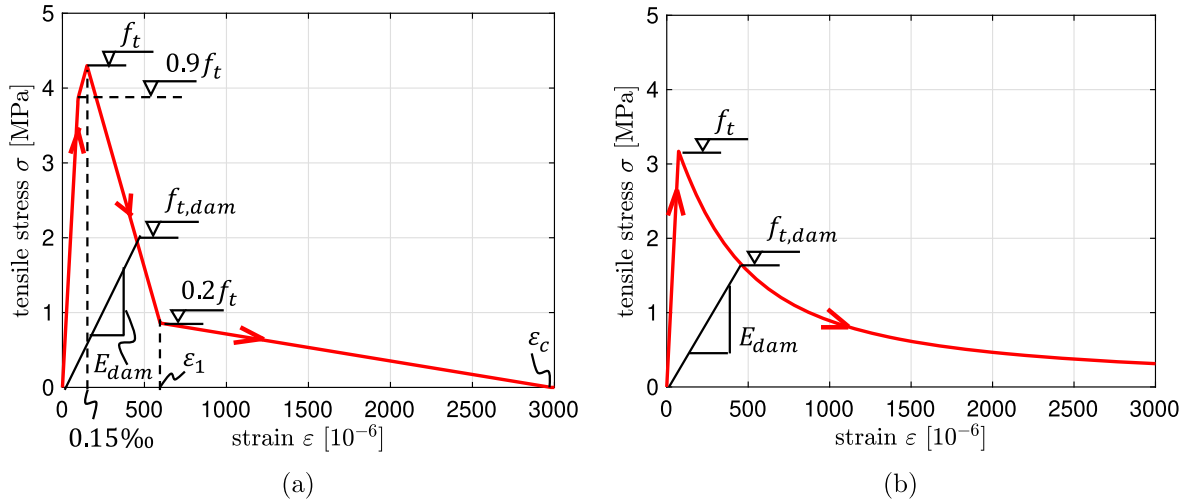

Fig. 5 Stress-strain diagrams for concrete in tension, computed (a) by the formulae of the *fib* Model Code (Taerwe and Matthys, 2013), where $\epsilon_1 = 0.000596$ and $\epsilon_c = 0.002980$ and (b) by the multiscale model by Hlobil (2016).

Notably, the values of the compressive strength of the concrete, obtained from the multiscale model and from the experiment, 62 MPa and 58 MPa, respectively, are close to each other. Thus the performance of the multiscale model by Königsberger *et al.* (2018) is satisfactory.

Homogenization of the uniaxial tensile strength and description of the progressive deterioration of the crack bands are based on the multiscale model by Hlobil (2016). It provides relations between the increase of the crack density ω and the decrease of the elastic stiffness E_{dam} and the tensile strength $f_{t,dam}$. The following results were obtained:

$$f_t = 3.17\text{MPa}, \tag{3}$$

$$E_{dam}(\omega) = \frac{1}{1 + 5.02\omega} \cdot E, \tag{4}$$

$$f_{t,dam}(\omega) = \sqrt{\frac{0.402}{0.402 + 0.396\omega}} \cdot f_t. \tag{5}$$

The combination of Eqs. (1) and (3)-(5) allows for determination of the stress-strain diagram for concrete in tension, see **Fig. 5(b)**.

Estimation of Effective Stiffnesses of Elements and of Crack Openings

Cracks of the segments were observed after load step 4. Consideration of these cracks requires subdivision of the segment into "simulation elements", see **Fig. 4**. The extensional stiffness and the bending stiffness of the undamaged lateral zones of the elements are equal to their initial values, determination of which is based on the Bernoulli-Euler hypothesis and on linear-elastic behavior of the concrete and steel, both in compression and tension. As for the crack band, the extensional stiffness and the bending stiffness are decreasing with increasing damage. Determination of the state of damage requires an incremental-iterative solution procedure, see details in (Zhang *et al.*, 2019a). Evaluation of the extensional stiffness and the bending stiffness of the crack band is based on (i) the Bernoulli-Euler hypothesis, (ii) linear-elastic behavior of steel, both in tension and in compression, and (iii) linear-elastic behavior of concrete in compression as well as on linear-elastic, nonlinear-softening of concrete in tension, see also **Fig. 5**. The effective extensional stiffness, $\overline{EA}^{(e)}$, and bending stiffness, $\overline{EI}^{(e)}$, of the corresponding elements $e = 1, 2, \ldots, 34$ are obtained by means of Voigt-Reuss-Hill estimates (Hill, 1952).

Crack opening at the surface of the elements, $w_c^{(e)}$, is estimated by multiplying the normal strain at the cracked surface of the corresponding crack band, $\varepsilon_{suf}^{(e)}$, by the size of this zone, l_{cb}, i.e.,

$$w_c^{(e)} = l_{cb} \cdot \varepsilon_{suf}^{(e)}. \tag{6}$$

Evaluation of $\varepsilon_{suf}^{(e)}$ is based on the Bernoulli-Euler hypothesis. It implies that a linear distribution of the normal strain in the tangential direction prevails inside every crack band. Thus,

$$\varepsilon_{suf}^{(e)} = \frac{\overline{N}^{(e)}}{\overline{EA}^{(e)} + \frac{\overline{M}^{(e)}}{\overline{EI}^{(e)}(r_{suf}^{(e)} - R)}}, \tag{7}$$

where $r_{suf}^{(e)} = [R + H/2; R - H/2]$ denotes the radial coordinate of the cracked surface, and $\overline{N}$ and $\overline{M}$ stand for the average axial force and the average bending moment over the simulation elements. The typical width of a crack band in the concrete, l_{cb}, suggested by Bažant and Oh (1983), amounts to three times the maximum aggregate size d_{max}, i.e.,

$$l_{cb} = 3d_{max}. \tag{8}$$

Therefore, the expression for the crack opening at the surface of the elements, $w_c^{(e)}$, is rewritten as

$$w_c^{(e)} = 3d_{max}\left[\frac{\overline{N}^{(e)}}{\overline{EA}^{(e)} + \frac{\overline{M}^{(e)}}{\overline{EI}^{(e)}(r_{suf}^{(e)} - R)}}\right]. \tag{9}$$

Transfer Relations as a Vehicle for Structural Analysis of Tunnel Rings

Segmental tunnel rings represent typical circular arch structures. Thus, the transfer relations, which are analytical solutions of the linear theory of circular arches, are used for structural analysis of such rings. These relations read as (Zhang *et al.*, 2017)

$$\begin{bmatrix} u(\varphi) \\ v(\varphi) \\ \theta(\varphi) \\ M(\varphi) \\ N(\varphi) \\ V(\varphi) \\ \hdashline 1 \end{bmatrix} = \left[\begin{array}{ccccccc} \cos\varphi & \sin\varphi & T_{13}(\varphi) & T_{14}(\varphi) & T_{15}(\varphi) & T_{16}(\varphi) & \sum u^L(\varphi) \\ -\sin\varphi & \cos\varphi & T_{23}(\varphi) & T_{24}(\varphi) & T_{25}(\varphi) & T_{26}(\varphi) & \sum v^L(\varphi) \\ 0 & 0 & 1 & T_{34}(\varphi) & T_{35}(\varphi) & T_{36}(\varphi) & \sum \theta^L(\varphi) \\ 0 & 0 & 0 & 1 & T_{45}(\varphi) & T_{46}(\varphi) & \sum M^L(\varphi) \\ 0 & 0 & 0 & 0 & \cos\varphi & -\sin\varphi & \sum N^L(\varphi) \\ 0 & 0 & 0 & 0 & \sin\varphi & \cos\varphi & \sum V^L(\varphi) \\ \hdashline 0 & 0 & 0 & 0 & 0 & 0 & 1 \end{array}\right] \begin{bmatrix} u_i \\ v_i \\ \theta_i \\ M_i \\ N_i \\ V_i \\ \hdashline 1 \end{bmatrix} \tag{10}$$

.

where

$$\begin{aligned}
&T_{13}(\varphi) = R sin\varphi, T_{14}(\varphi) = \frac{R^2}{EI}(cos\varphi - 1),\\
&T_{15}(\varphi) = \frac{R}{EA}\frac{1}{2}\varphi sin\varphi + \frac{R^3}{EI}\left(\frac{1}{2}\varphi sin\varphi + cos\varphi - 1\right),\\
&T_{16}(\varphi) = \frac{R}{EA}\left(\frac{1}{2}\varphi cos\varphi - \frac{1}{2}sin\varphi\right) + \frac{R^3}{EI}\left(\frac{1}{2}\varphi cos\varphi - \frac{1}{2}sin\varphi\right),\\
&T_{23}(\varphi) = R(cos\varphi - 1), T_{24}(\varphi) = \frac{R^2}{EI}(\varphi - sin\varphi),\\
&T_{25}(\varphi) = \frac{R}{EA}\left(\frac{1}{2}\varphi cos\varphi + \frac{1}{2}sin\varphi\right) + \frac{R^3}{EI}\left(\varphi - \frac{3}{2}sin\varphi + \frac{1}{2}\varphi cos\varphi\right),\\
&T_{26}(\varphi) = \frac{R}{EA}\left(-\frac{1}{2}\varphi sin\varphi\right) + \frac{R^3}{EI}\left(1 - cos\varphi - \frac{1}{2}\varphi sin\varphi\right),\\
&T_{34}(\varphi) = -\frac{R}{EI}\varphi, T_{35}(\varphi) = \frac{R^2}{EI}(sin\varphi - \varphi), T_{36}(\varphi) = \frac{R^2}{EI}(cos\varphi - 1),\\
&T_{45}(\varphi) = R(1 - cos\varphi), T_{46}(\varphi) = R sin\varphi.
\end{aligned} \tag{11}$$

The vector on the left-hand-side of Eq. (10) contains the kinematic and static variables, referring to the cross-section at an arbitrary value of the angular coordinate φ. These variables are the radial displacement u, the tangential displacement v, the cross-sectional rotationθ, the bending moment M, the axial force N, and the shear force V. The vector on the right-hand-side of Eq. (10) contains the kinematic and static variables, referring to the initial cross-section (index "i"), i.e. $\varphi = 0$. These six quantities are the integration constants. Three of them, representing kinematic quantities, may be set equal to zero, i.e., $u_i = v_i = \theta_i = 0$. This is admissible because they describe rigid body displacement of the ring (Zhang *et al.*, 2019a). The three remaining integration constants, representing static quantities, are determined from three continuity conditions of a closed ring. The seven-by-seven matrix on the right-hand-side of Eq. (10) is the transfer matrix. The top-left six-by-six submatrix of this matrix represents the solution for an unloaded part of the segmental tunnel ring (Zhang *et al.*, 2017). The top six elements of the last column of the

transfer matrix stand for the superposition of so-called "load integrals" (superscript "L"). The latter represent analytical solutions for specific types of generalized loads. Load integrals for dead load, interfacial discontinuities of kinematic variables, and for point loads are given in Zhang *et al.* (2017). Load integrals for a uniform temperature change, ground pressure, and for the overload on the ground surface are given in Zhang *et al.* (2018), (2019b) and Zhang *et al.* (2021), respectively.

In this contribution, the hybrid method, developed by Zhang *et al.* (2017), (2019a), is employed for re-analysis of the real-scale test of the segmental tunnel ring, performed by Liu *et al.* (2016). The test was carried out in a force-controlled fashion. Compressive loading was imposed by 24 hydraulic jacks, resulting in point loads acting on the outer surface of the ring. The tangential displacement discontinuities across both the inner and the outer gaps of the joints and the vertical and the horizontal convergences were experimentally monitored. The hybrid method requires as input for the analysis (1) the point loads, imposed by the hydraulic jacks, and (2) the relative rotation angles at the joints, estimated from the measured displacement discontinuities.

The load integrals for a radial point load P, imposed at the position φ_p, read as (Zhang *et al.*, 2017):

$$u^L(\varphi) = \frac{1}{2}\left(\frac{PR}{EA} + \frac{PR^3}{EI}\right)\Big[sin(\varphi - \varphi_p) - (\varphi - \varphi_p)cos(\varphi - \varphi_p)\Big]H(\varphi - \varphi_p)\,, \tag{12}$$

$$\begin{aligned} v^L(\varphi) = {} & \frac{PR}{EA}\left[\frac{1}{2}\Big(\varphi - \varphi_p\Big)sin\Big(\varphi - \varphi_p\Big)\right]H\Big(\varphi - \varphi_p\Big) \\ & + \frac{PR^3}{EI}\left[\frac{1}{2}\Big(\varphi - \varphi_p\Big)sin\Big(\varphi - \varphi_p\Big) + cos\Big(\varphi - \varphi_p\Big) - 1\right]H\Big(\varphi - \varphi_p\Big)\,, \end{aligned} \tag{13}$$

$$\theta^L(\varphi) = \frac{PR^2}{EI}[1 - cos(\varphi - \varphi_p)]H(\varphi - \varphi_p)\,, \tag{14}$$

$$M^L(\varphi) = -RPsin(\varphi - \varphi_p)H(\varphi - \varphi_p)\,, \tag{15}$$

$$N^L(\varphi) = Psin(\varphi - \varphi_p)H(\varphi - \varphi_p)\,, \tag{16}$$

$$V^L(\varphi) = -Pcos(\varphi - \varphi_p)H(\varphi - \varphi_p)\,, \tag{17}$$

where $H(\varphi - \varphi_j)$ stands for the Heaviside function. The load integrals for the relative rotation angle, $\Delta\theta_j$, at the joint located at $\varphi = \varphi_j$, read as (Zhang *et al.*, 2017)

$$u^L(\varphi) = -R\Delta\theta_j sin(\varphi - \varphi_j)H(\varphi - \varphi_j)\,, \tag{18}$$

$$v^L(\varphi) = R\Delta\theta_j\Big[1 - cos(\varphi - \varphi_j)\Big]H(\varphi - \varphi_j)\,, \tag{19}$$

$$\theta^L(\varphi) = \Delta\theta_j H(\varphi - \varphi_j)\,, \tag{20}$$

$$N^L(\varphi) = V^L(\varphi) = M^L(\varphi) = 0\,. \tag{21}$$

Assessment of the Added Value of Multiscale Structural Analysis Concerning the Prediction of Cracking

The assessment of the added value of multiscale modeling of concrete for structural analysis of segmental tunnel rings is based on the comparison of experimental data with results from both conventional and multiscale structural analysis, see **Fig. 1**. The focus is on two types of quantities that are relevant to the serviceability and the durability of tunnel linings:

(1) The convergences in the vertical and the horizontal direction,
(2) The opening widths of bending-induced cracks of concrete.

The experimental data refer to the first ten load steps of the previously mentioned real-scale test of a segmental tunnel ring, performed by Liu *et al.* (2016). These steps are associated with the increase of the external loading of the tunnel ring up to the level that simulates the ground pressure acting on the extrados of tunnel linings in the expected practical service (Liu *et al.*, 2016).

Two modes of structural analysis were carried out. The first one is a conventional structural analysis based on the *fib* Model Code, see the Appendix for the relevant formulae. The second one is a multiscale structural analysis based on the multiscale models for concrete, presented in Section "Evaluation of the Material Properties of Concrete by Means of Multiscale Modeling". Both modes of analysis were nonlinear hybrid computations. They are *hybrid*, insofar as experimental data regarding the external loading *and* displacement measurements at the joints are used as input. They are *nonlinear*, because bending-induced cracking of the reinforced concrete segments is accounted for. Despite this nonlinearity, structural analysis can be subdivided into two load cases (Zhang *et al.*, 2019a). Load case I is concerned with the computation of the deformation of the segments of the tunnel ring, resulting from external loading, while the relative rotations at the joints are set equal to zero. Load case II aims at determination of rigid body displacements of the segments of the tunnel ring, resulting from the relative rotations at the joints. After estimation of these rotations based on the experimentally measured displacement discontinuities at the joints, they are postprocessed such that symmetric rigid body displacements of the segments are obtained (Zhang *et al.*, 2019a). In the given case, the restriction to

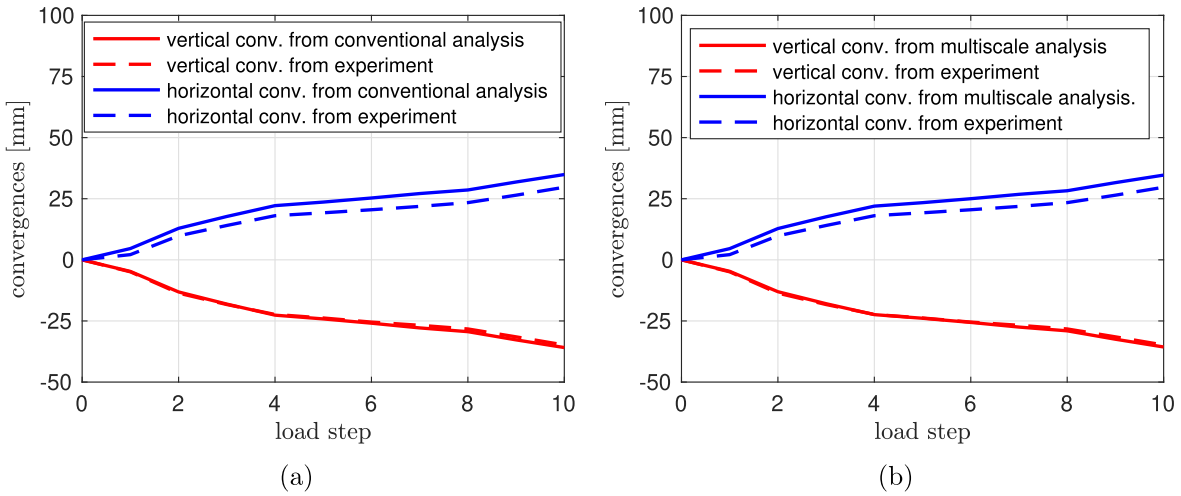

Fig. 6 Comparison of the convergences obtained from experimental measurements with those from (a) conventional structural analysis and (b) multiscale structural analysis.

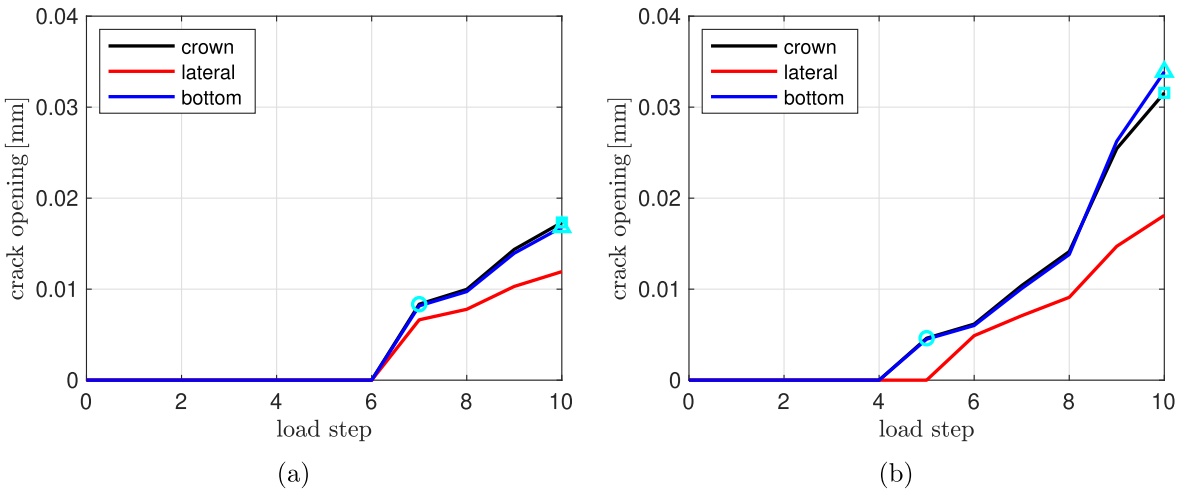

Fig. 7 Crack openings at the surface of the segments in the top element, the lateral element, and the bottom element, as a function of the load step: (a) conventional structural analysis and (b) multiscale structural analysis.

symmetric rigid body displacements is adequate, because the observed structural behavior was indeed virtually symmetric. This renders the available extension towards consideration of both symmetric *and* antisymmetric modes of rigid body displacements dispensable (Jiang *et al.*, 2021). Despite the nonlinearity of the material behavior in load case I, superposition of the results from the two load cases is admissible, because load case II only produces rigid body displacements and because the equilibrium equations are formulated for the undeformed configuration. This completes the nonlinear hybrid analysis.

As for the vertical and horizontal convergences, both conventional and multiscale structural analyses deliver very similar predictions which agree well with corresponding experimental measurements, see **Fig. 6**. Thus, both modes of structural analysis are useful. The added value resulting from the use of the multiscale model for concrete is insignificant. This was expected, because the convergences are governed by rigid body displacements resulting from the relative rotations at the joints, while the deformations of the segments is less important (Zhang *et al.*, 2019a).

As regards bending-induced cracks of concrete, the two modes of nonlinear hybrid analysis deliver different results. Conventional structural analysis indicates that cracking initiates at load step 7, see the cyan circle in **Fig. 7(a)**. In the experiments, however, cracking was observed already at load step 5. Thus, conventional structural analysis overestimates the external loading at crack initiation by some 55%. Multiscale structural analysis, however, indicates that cracking starts already at load step 5, see the cyan circle in **Fig. 7(b)**. This underlines the added value resulting from use of the multiscale model for concrete, as compared to the standard approach based on the *fib* Model Code. As for the final load step, i.e., load step 10, multiscale structural analysis results in crack opening widths at the crown and the bottom of the ring, which are approximately twice as large as the values obtained from conventional structural analysis, see the cyan squares and triangles in **Fig. 7**. Also the crack lengths are significantly different. In

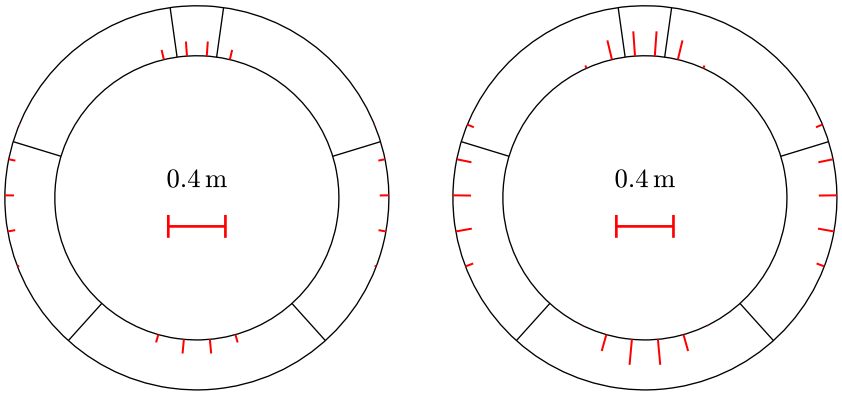

Fig. 8 Crack lengths at the final load step 10: obtained from (a) conventional structural analysis and (b) multiscale structural analysis.

case of conventional standard analysis, the maximum crack length is obtained in the region of the crown. It amounts to 10.2 cm, see **Fig. 8(a)**. In case of multiscale analysis, the maximum crack length is obtained at the bottom of the ring. It amounts to 17.9 cm, see **Fig. 8(b)**. It is concluded that multiscale structural analysis allows for a more realistic and more conservative durability assessment of segmental tunnel linings. The larger the crack opening widths and the larger the crack lengths, the higher is the risk that aggressive substances enter the segments and initiate corrosion of the steel reinforcement.

Thus, multiscale structural analysis is preferable for a durability-oriented design of segmental tunnel rings.

Conclusions

In order to assess the added value of multiscale structural analysis of segmental tunnel rings relative to a conventional mode of structural analysis, a real-scale test of a segmental tunnel ring, performed by Liu *et al.* (2016), was analyzed. The following conclusions are drawn from this analysis:

(1) The input for the multiscale model for a customized concrete, used in this work, refers to its initial composition, defined by the mix design, and the maturity of the material, typically quantified by means of hydration degrees. Thus, efforts concerning material tests are superfluous. This is one of the merits of the multiscale model as compared to the *fib* Model Code.
(2) Both conventional and multiscale structural analysis are equally reliable concerning estimation of the convergences. In that case, the added value of the multiscale structural analysis is insignificant, because the convergences are predominately governed by rigid body displacements of the segments, resulting from the relative rotation angles at the joints (Zhang *et al.*, 2019a), rather than by the deformation of the segments, which increases with bending-induced cracking of concrete.
(3) Multiscale structural analysis resulted in correct predictions of the initiation of cracking of concrete. Results from conventional structural analysis, however, overestimated the level of the external loading at onset of cracking by some 55%. This underlines the added value of multiscale structural analysis. The difference between the two compared modes of structural analysis is significant for the long-term durability of segmental tunnel linings with a designed service life of 100 years and more.

Acknowledgments

Financial support by the Austrian Science Fund (FWF), provided for the project P 281 31-N32 "Bridging the Gap by Means of Multiscale Structural Analyses", is gratefully acknowledged. In addition, the first author is indebted to the National Natural Science Foundation of China (Grant No. 51908424), the Shanghai Pujiang Program (Grant No. 19PJ1409700), and to the Austrian Federal Ministry of Education, Science and Research (BMBWF) (Grant No. ICM-2019–14045) for financial support of this work. The third author is also indebted to the National Natural Science Foundation of China (Grant No. 51578409), for financial support of this work.

Appendix: Quantification of the Tensile Strength and of Softening of Concrete According to *fib* Model Code 2010 (Taerwe and Matthys, 2013)

The experimentally determined compressive strength of concrete, f_c, was equal to 58 MPa. Based on this value, the *fib* Model Code contains the following formulae for quantification of the tensile strength, f_t, the elasticity modulus, E, and the fracture energy, G, of concrete,

$$f_t = 2.12 \cdot ln[1 + 0.1(f_c + 8)] = 4.30 MPa, \tag{A.1}$$

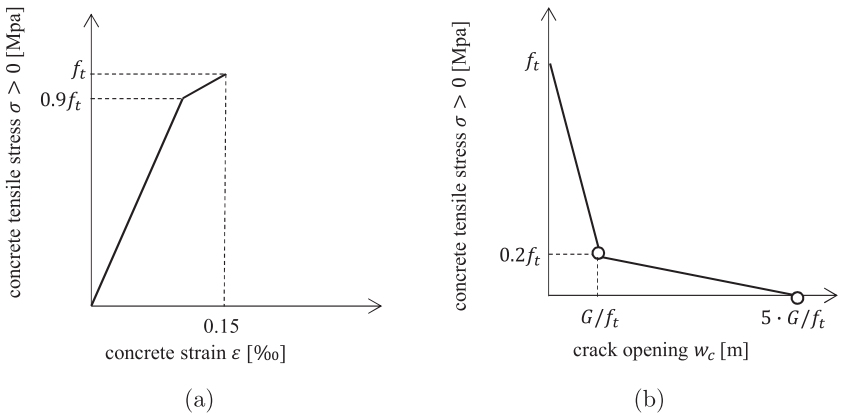

Fig. A. 1 Schematic representation of the stress-strain and stress - crack opening relation for uniaxial tension, according to the *fib* Model Code 2010: (a) uncracked concrete and (b) cracked concrete. Reproduced from Taerwe, L., Matthys, S., 2013. *fib* Model Code for Concrete Structures 2010. Wiley (Ernst & Sohn).

$$E = 21.5 \cdot 1.0 \cdot \left(\frac{f_c + 8}{10}\right)^{1/3} = 40330 MPa, \tag{A.2}$$

$$G = 0.73 \cdot f_c^{0.18} = 154 N/m. \tag{A.3}$$

For uncracked concrete, the *fib* Model Code suggests a bilinear curve, see **Fig. A.1(a)**, describing the stress-strain relation. As for cracked concrete, another bilinear curve, see **Fig. A.1(b)**, describing the relation of the tensile stress and the crack opening, is given. Notably, the combination of Eqs. (6) and (8) allows for the evaluation of the tensile strain as a function of the crack opening. Considering Eqs. (A.1)–(A.3), (6), (8), $d_{max} = 0.02$ m, the stress-strain and the stress-crack opening relation, illustrated in **Fig. A.1**, results in a piecewise-linear curve, describing the stress-strain relation of both the uncracked and the cracked concrete in tension, see **Fig. 5(a)**.

The mathematical expressions for this stress-strain relation read as

$$\sigma = \begin{cases} E\varepsilon & \ldots 0 < \varepsilon \leq \dfrac{0.9f_t}{E}, \\ 0.9f_t + \dfrac{0.1f_t}{0.00015 - 0.9f_t/E}\left(\varepsilon - \dfrac{0.9f_t}{E}\right) & \ldots \dfrac{0.9f_t}{E} < \varepsilon \leq 0.00015, \\ f_t - \dfrac{0.8f_t}{\varepsilon_1 - 0.00015}(\varepsilon - 0.00015) & \ldots 0.00015 < \varepsilon \leq \varepsilon_1, \\ 0.2f_t - \dfrac{0.2f_t}{\varepsilon_c - \varepsilon_1}(\varepsilon - \varepsilon_1) & \ldots \varepsilon_1 < \varepsilon \leq \varepsilon_c, \\ 0 & \ldots \varepsilon > \varepsilon_c, \end{cases} \tag{A.4}$$

where $\varepsilon_1 = G/f_t = 0.000596$ and $\varepsilon_c = 5 \cdot G/f_t = 0.0029780$.

References

Bažant, Z.P., Oh, B.H., 1983. Crack band theory for fracture of concrete. Materials and Structures 16, 155–177.

Benveniste, Y., 1987. A new approach to the application of Mori-Tanaka's theory in composite materials. Mechanics of materials 6, 147–157.

Bernard, O., Ulm, F.J., Lemarchand, E., 2003. A multiscale micromechanics-hydration model for the early-age elastic properties of cement-based materials. Cement and Concrete Research 33, 1293–1309.

Cui, J.Z., Yang, H., 1996. A dual coupled method for boundary value problems of PDE with coefficients of small period. Journal of Computational Mathematics 14, 159–174.

Geers, M., Kouznetsova, V., Brekelmans, W., 2010. Multi-scale computational homogenization: Trends and challenges. Journal of Computational and Applied Mathematics 234, 2175–2182.

Hellmich, C., Mang, H., 2005. Shotcrete elasticity revisited in the framework of continuum micromechanics: From submicron to meter level. Journal of Materials in Civil Engineering 17, 246–256.

Hershey, A., 1954. The elasticity of an isotropic aggregate of anisotropic cubic crystals. Journal of Applied Mechanics-Transactions (ASME) 21, 236–240.

Hill, R., 1952. The elastic behaviour of a crystalline aggregate. Proceedings of the Physical Society. Section A 65, 349–354.

Hlobil, M., 2016. Micromechanical Analysis of Blended Cement-Based Composites. (Ph.D. thesis). Vienna University of Technology, Austria, and Czech Technical University in Prague, Czech Republic.

Jiang, Z., Liu, X., Schlappal, T., *et al.*, 2021. Asymmetric serviceability limit states of symmetrically loaded segmental tunnel rings: hybrid analysis of real-scale tests. Tunnelling and Underground Space Technology. (In print).

Königsberger, M., Hlobil, M., Delsaute, B., *et al.*, 2018. Hydrate failure in ITZ governs concrete strength: A micro-to-macro validated engineering mechanics model. Cement and Concrete Research 103, 77–94.

Königsberger, M., Hassan, Irfan-ul, Pichler, M., Hellmich, C, B., 2016. Downscaling based identification of nonaging power-law creep of cement hydrates. Journal of Engineering Mechanics 142.04016106.

Kröner, E., 1958. Berechnung der elastischen Konstanten des Vielkristalls aus den Konstanten des Einkristalls [Computation of the elastic constants of a polycrystal based on the constants of the single crystal]. Zeitschrift für Physik 151, 504–518.
Liu, X., Bai, Y., Yuan, Y., Mang, H., 2016. Experimental investigation of the ultimate bearing capacity of continuously jointed segmental tunnel linings. Structure and Infrastructure Engineering 12, 1364–1379.
Lumley, J., Gollop, R., Moir, G., Taylor, H., 1996. Degrees of reaction of the slag in some blends with Portland cements. Cement and Concrete Research 26, 139–151.
Mang, H., 2015. Bridging the gap by means of multiscale structural analyses, Research project supported by the Austrian Science Fund (FWF) P281 131/N32.
Mori, T., Tanaka, K., 1973. Average stress in matrix and average elastic energy of materials with misfitting inclusions. Acta metallurgica 21, 571–574.
Pichler, B., Hellmich, C., 2011. Upscaling quasi-brittle strength of cement paste and mortar: A multi-scale engineering mechanics model. Cement and Concrete Research 41, 467–476.
Pichler, C., Lackner, R., Mang, H.A., 2007. A multiscale micromechanics model for the autogenous-shrinkage deformation of early-age cement-based materials. Engineering Fracture Mechanics 74, 34–58.
Scheiner, S., Hellmich, C., 2009. Continuum microviscoelasticity model for aging basic creep of early-age concrete. Journal of Engineering Mechanics 135, 307–323.
Schlangen, E., 1993. Experimental and Numerical Analysis of Fracture Processes in Concrete. (Ph.D. thesis). The Netherlands: Delft University of Technology.
Taerwe, L., Matthys, S., 2013. *fib* Model Code for Concrete Structures 2010. Wiley. (Ernst & Sohn).
Termkhajornkit, P., Vu, Q.H., Barbarulo, R., Daronnat, S., Chanvillard, G., 2014. Dependence of compressive strength on phase assemblage in cement pastes: Beyond gel - space ratio - Experimental evidence and micromechanical modeling. Cement and Concrete Research 56, 1–11.
Wang, H., Binder, E., Mang, H., Yuan, Y., Pichler, B., 2018a. Multiscale structural analysis inspired by exceptional load cases concerning the immersed tunnel of the Hong Kong-Zhuhai-Macao Bridge. Underground Space 3, 252–267.
Wang, H., Hellmich, C., Yuan, Y., Mang, H., Pichler, B., 2018b. May reversible water uptake/release by hydrates explain the thermal expansion of cement paste? - Arguments from an inverse multiscale analysis. Cement and Concrete Research 113, 13–26.
Zaoui, A., 2002. Continuum micromechanics: Survey. Journal of Engineering Mechanics 128, 808–816.
Zhang, J.L., Vida, C., Yuan, Y., *et al.*, 2017. A hybrid analysis method for displacement-monitored segmented circular tunnel rings. Engineering Structures 148, 839–856.
Zhang, J.L., Liu, X., Yuan, Y., Mang, H., 2015. Multiscale modeling of the effect of the interfacial transition zone on the modulus of elasticity of fiber-reinforced fine concrete. Computational Mechanics 55, 37–55.
Zhang, J.L., Liu, X., Yuan, Y., Mang, H.A., Pichler, B.L.A., 2020. Transfer relations as the basis for computer-aided engineering of circular arch structures. Engineering Computations. https://doi.org/10.1108/EC-06-2020-0313.
Zhang, J.L., Liu, X., Zhao, J., Mang, H., 2021. A combined precast and in-situ-cast construction method for large-span underground vaults. Tunnelling and Underground Space Technology 111, 103795.
Zhang, J.L., Hellmich, C., Mang, H.A., Yuan, Y., Pichler, B., 2018. Application of transfer relations to structural analysis of arch bridges. Computer Assisted Methods in Engineering and Science 24, 199–215.
Zhang, J.L., Mang, H.A., Liu, X., Yuan, Y., Pichler, B., 2019a. On a nonlinear hybrid method for multiscale analysis of a bearing-capacity test of a real-scale seg-mental tunnel ring. International Journal for Numerical and Analytical Methods in Geomechanics 43, 1343–1372.
Zhang, J.L., Schlappal, T., Yuan, Y., Mang, H.A., Pichler, B., 2019b. The influence of interfacial joints on the structural behavior of segmental tunnel rings subjected to ground pressure. Tunnelling and Underground Space Technology 84, 538–556.
Zhang, Y., Pichler, C., Yuan, Y., Zeiml, M., Lackner, R., 2013. Micromechanics-based multifield framework for early-age concrete. Engineering Structures 47, 16–24.